FRACTURE SIMULATION OF CONSTRUCTIONAL STEELS IN TWO FRACTURE MODES

Shen YAN [a, b], Kim J. R. RASMUSSEN [a] and Xianzhong ZHAO [b]

[a] School of Civil Engineering, the University of Sydney, Sydney, Australia
Emails: shen.yan@sydney.edu.au, kim.rasmussen@sydney.edu.au

[b] College of Civil Engineering, Tongji University, Shanghai, China
Emails: x.zhao@tongji.edu.cn

Keywords: Fracture model; Steel material; Stress-strain relationship; Coupon test; Microscopic mechanism.

Abstract: *The paper presents a comprehensive study, aiming to provide useful tools for numerically predicting the fracture phenomenon in steel structures. A micro-mechanically-based fracture model is proposed, which comprises two competing and correlated fracture criteria corresponding to the shear and tension fracture modes. Yield-to-fracture strain hardening behaviour of constructional steel is also investigated, and numerical modelling technique for fracture simulation in implicit time integration analysis is addressed. Having setting out all necessary components, coupon tests covering a wide range of stress states are carried out and numerically simulated to calibrate and validate the fracture model. Numerical results agree well with the experimental results, and conclusions are drawn about the suitability of the proposed fracture model and methods for predicting fracture in both shear and tension modes.*

1. INTRODUCTION

Fracture governs the ultimate strength of most steel connections and is a major failure mode for steel structures. Two significant characteristics of fracture are observed in steel structures. For one thing, constructional steels are typical ductile metals, and thus in structures without geometrical flaws, fracture normally occurs with the presence of large-scale yielding. Hence, traditional fracture mechanics, which are developed on presumption of the already existing macroscopic crack, are difficult to be employed under such circumstance. Meanwhile, it is desired to precisely obtain the yield-to-fracture strain hardening behaviour, such that the plastic deformation field in the vicinity of the potential fracture locations can be accurately calculated. For another thing, fracture normally initiates at stress-concentration or geometry-discontinuous locations, where the stress states can be very different, and thereby fracture can initiate and propagate in both tension and shear modes. This necessitates the development of fracture models that allow for both shear and tension failure of constructional steels.

The paper first investigates the yield-to-fracture strain hardening behaviour of steel material, by means of comprehensive tests on standard tension coupons and theoretical derivations. Then, a fracture model for ductile metal is proposed, which readily applies to constructional steel. The fracture model is based on material behaviour on microscopic level, i.e., the evolution of microscopic voids under various stress states. Furthermore, numerical technique of fracture simulation in implicit time integration analysis is also addressed.

Finally, coupon tests representing different stress states are carried out and numerically simulated to calibrate and validate the proposed fracture model for Q345 grade steel. Conclusion is drawn about the excellent performance of the proposed fracture model and methods. Further details can be found in [1-3].

2. YIELD-TO-FRACTURE TRUE STRESS-STRAIN RELATIONSHIP

2.1 Current methods

When the research interest of steel structures shifts from the elastic response to the ultimate strength and fracture behaviour, material strain hardening is of significant importance because it directly affects both the plastic flow stress, which determines the structural resistance at plastic stage, and the plastic deformation, which is accumulated until necessary for fracture to initiate. Standard tension coupon tests give values of nominal stress, s, and nominal strain, e. True stress, σ, and true strain, ε, then can be obtained through:

$$\varepsilon = \ln\left(1+e\right) \tag{1}$$

$$\sigma = s\left(1+e\right) \tag{2}$$

Necking of coupon occurs when the material hardening cannot compensate the geometric softening. After necking occurs, the deformation within the gauge length is no longer uniform, such that the nominal strain measured from gauge reading is not the real nominal strain but an "averaged" strain within the gauge length, making Eqs. (1) and (2) no longer valid in the post-necking range. In practical applications where post-necking stress-strain relationship is desired, most studies followed the research by Bridgeman [4], assuming a positive constant hardening modulus for the entire post-necking range. It is natural instinct to obtain the post-necking stress-strain relationship by connecting the stress-strain point at necking to that at fracture. Many researchers calculated stress and strain at fracture through:

$$\sigma = \frac{P}{A} \tag{3}$$

$$\varepsilon = \ln\frac{A_0}{A} \tag{4}$$

where P is taken as P_f, the pulling force recorded when the pulling of coupon lose stability, A is taken as A_f, the cross-sectional area of the neck of the coupon measured after the whole coupon fractures, and A_0 is the original cross-sectional area of the coupon. Note that P_f and A_f are from different stages of test (stage of P_f is earlier than stage of A_f) and the coupon neck continues to shrink after the pulling force reaches P_f. Hence, the fracture stress calculated by Eq. (3) is obviously larger than the real value. More significantly, the fracture of the tension coupon is a process that initiates at the core of the coupon neck and then propagates across the entire cross section of the neck. Material fracture (fracture of an infinitesimal material point at the neck core) occurs prior to the fracture of the whole coupon, making the real fracture strain almost impossible to obtain because it is difficult to know the exact moment of fracture initiation inside a coupon.

In order to circumvent the problem of finding the real fracture stress and strain, other researchers adopted a numerical trial-and-error method to find the post-necking hardening modulus, namely, by assuming different post-necking hardening moduli, the tensile coupon

test was numerically simulated until a suitable modulus is found to allow a good agreement between the simulation and test results. Not only heavily dependent on the numerical technique, this method is also complex and cost inefficient.

2.2 Tests of standard tension coupons

A series of standard coupon (smooth round bar, SRB) tests were carried out, with a special focus on the post-necking strain hardening behaviour and the fracture stress and strain. Sixteen SRB coupons made from Q345 grade steel to GB 50017 [5] were tested using MTS-810 Material Testing System at quasi-static loading rates under displacement-control mode. All coupons shared identical geometries shown in Fig. 1.
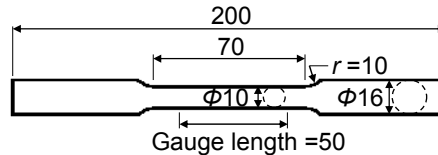

Fig. 1 Geometries of SRB coupon (unit: mm).

Coupons SRB-1 to SRB-3 were loaded to fracture to obtain the nominal stress-strain (*s-e*) relationship. An average stress-strain curve was determined by simple averaging. For coupons SRB-4 to SRB-14, each of them was loaded to a target nominal strain ranging from necking stage to fracture stage, as shown in Fig. 2. The contour geometries of the neck of the coupons, including the radius of the cross section of the neck, r, and the radius of curvature of the arc profile at the neck, R, were measured using Mitutoyo-QS250Z Non-Contact Vision Measuring Machine. Coupons SRB-15 and SRB-16 were used to experimentally determine the moment of fracture initiation at the core of the neck, which marked material fracture. The loading of each coupon was switched to force-control mode just prior to complete coupon fracture, and was halted when the force reduced to a target value, as shown in Fig. 3. The neck region was mechanically cut out and then was cut into halves along the longitudinal direction. The cutting planes were polished and observed through an electric magnifier. No crack was found in SRB-15, while a zigzag crack was observed at the core of SRB-16.
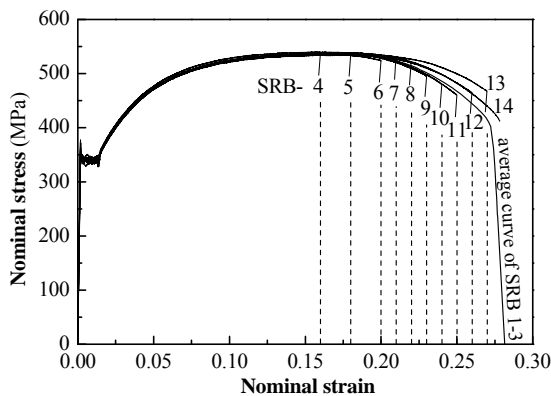

Fig. 2 Nominal stress-strain curves of SRB coupons.
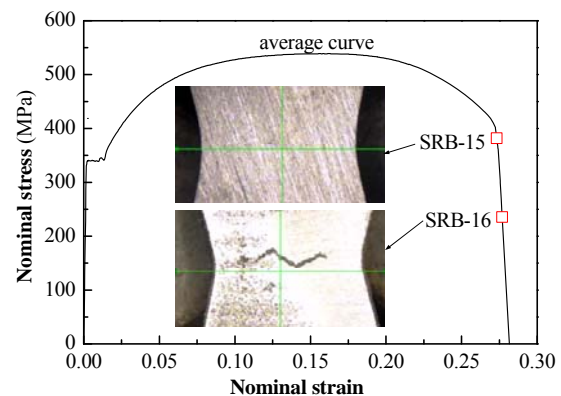

Fig. 3 Coupon neck core observation.

2.3 True stress-strain relationship

Equations (1) and (2) convert nominal stress and strain to true stress and strain, but only hold before necking of coupon occurs, as previously discussed. Necking initiates when

$$\frac{\mathrm{d}s}{\mathrm{d}e} = 0 \qquad (5)$$

Equation (5) determines the necking nominal stress, s_{nk}, and nominal strain, e_{nk}. After necking has occurred, the true stress and strain at the neck can be calculated according to Eqs. (3) and (4), i.e., using the real-time cross-sectional area of the neck instead of using the deformation of the gauge length. But in actuality, the stress across the neck cross section is also non-uniform, and Eq. (3) only gives an average stress at the neck. By presuming a uniformly longitudinal plastic strain distribution and a circular arc profile at the neck, an approximate stress field in the close vicinity of the neck was obtained in [4], based on which the true stress at the core of the coupon neck is:

$$\sigma = \frac{P / \pi r^2}{\left(1 + \dfrac{2R}{r}\right) \ln\left(1 + \dfrac{r}{2R}\right)} \qquad (6)$$

Figure 4 plots the scattered true stress-strain pairs that were calculated from coupons SRB-4 to SRB-14 through Eqs. (4) and (6). A constant hardening modulus gives a good fitting of the scattered points, which is in accordance with the previous studies on other ductile metals [4]. Hence, the post-necking true stress-strain relationship can be written as:

$$\sigma = \sigma_{nk} + \zeta \cdot \sigma_{nk} \left(\varepsilon - \varepsilon_{nk}\right) \qquad (7)$$

where σ_{nk} and ε_{nk} are the true stress and strain when necking starts, respectively, and ζ is defined as the post-necking hardening parameter. For Q345 grade steel, σ_{nk}, ε_{nk} and ζ equal to 625 MPa, 0.145 and 0.62, respectively.
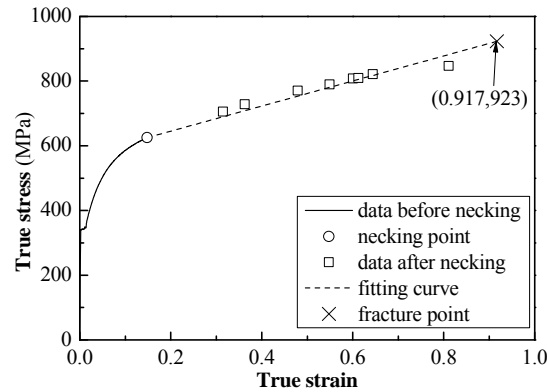

Fig. 4 True stress-strain relationship of Q345 grade steel.

Note again this study investigates the fracture behaviour on the material level, namely, fracture of an infinitesimal material point rather than fracture of the entire coupon. A simple method is put forward to calculate the strain at the inner core of the coupon neck when fracture starts to initiate there. In the SRB tests, the pulling forces dropped abruptly near the end of the tests due to crack propagation across the cross section of the coupon neck. Hence, the starting point of the unstable pulling reflected the initiation of material fracture at the neck core. It is also observed that the unstable pulling forces P_f were almost constant in different coupon tests, and therefore, P_f provides a useful determinant for fracture strain calculation.

Equating Eqs. (6) and (7), and assuming a linear relationship between r/R ratio and true strain, namely, $r/R = \eta(\varepsilon - \varepsilon_{nk})$, which was noticed in the tests, the post-necking true strain is related to the pulling force by:

$$\frac{P \cdot \mathrm{e}^{\varepsilon}}{\pi r_0^2 \sigma_{nk}\left(1 + \dfrac{2}{\eta(\varepsilon - \varepsilon_{nk})}\right)\ln\left(1 + \dfrac{\eta(\varepsilon - \varepsilon_{nk})}{2}\right)} - \zeta(\varepsilon - \varepsilon_{nk}) = 1 \tag{8}$$

For Q345 grade steel, coupon tests showed that P_f was about 31.5 kN, and thus ε_f was calculated as 0.917. It is noted that ε_f calculated above was between the true strains of SRB-15 and SRB-16, 0.907 and 0.962, respectively, demonstrating excellent accuracy of Eq. (8).

2.4 Recommended procedure of standard tension coupon tests

The above tests and analysis enable accurate calculation of the plastic and fracture properties of a ductile metal. However, usage of sixteen coupons makes the above procedure difficult to apply. A simplified experimental procedure is provided, requiring tests of only two SRB coupons. In this simplified procedure, only one SRB coupon instead of three coupons (SRB-1 to SRB-3) is used to obtain the nominal stress-strain curve, and only one SRB coupon instead of eleven coupons (SRB-4 to SRB-14) is adopted to measure the contour geometries of the neck, which are used to calculate parameters ζ and η. Detailed procedure and equations can be found in [1, 2].

3. MICRO-MECHANISM-BASED FRACTURE MODEL

3.1 Assumptions

Research into the microscopic structures of ductile metals showed that, microscopic voids form at the inclusions and second phase particles when the material is loaded, and material fracture results from the nucleation, growth and coalescence of the voids [6]. If the voids can nucleate with little difficulty, the fracture process is dominated by the growth and coalescence of voids; otherwise, void nucleation is the critical step, i.e., fracture occurs soon after the nucleation of voids. Overwhelming evidence showed that tension fracture under high stress triaxiality T, which is a non-dimensional representation of the hydrostatic stress σ_h by defining $T = \sigma_h/\sigma_{eq}$ where σ_{eq} is the equivalent von Mises stress, belongs to the former situation. This is the microscopic mechanism of tension fracture, which is well acknowledged.

Difficulty of void nucleation increases with the decrease of hydrostatic stress [7, 8], and thus void nucleation process shall play a more significant role in shear fracture in low positive and negative triaxiality regime. Moreover, observation of the shear failure surface showed that, after nucleation voids change their shapes and collapse abruptly, leading to the formation of shear band and the final fracture in shear [9]. Therefore, it is assumed that the strain to fracture under low positive and negative triaxiality, ε_f^s, can be calculated as:

$$\varepsilon_f^s = c_1 \varepsilon_{nc} \cdot c_2 \varepsilon_{cl} \tag{9}$$

where ε_{nc} is the equivalent plastic strain needed for the voids to nucleate, ε_{cl} is the critical strain leading to collapse of the voids and formation of the localized shear band, and c_1 and c_2 are corresponding coefficients.

3.2 Tensile fracture criterion

After voids nucleate in ductile metal, the initial volume fraction is still very small, such that each void evolves independently, which can be investigated by studying a cubic that contains a spherical void located at its centre. Such analysis is called "unit cell-based micromechanical study" [10].
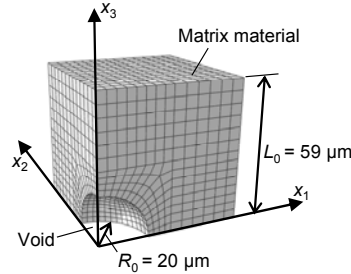

Fig. 5 Finite-element model of 1/8 of a unit cell.

Finite-element model of 1/8 of the cubic cell (due to the three-fold symmetry) is developed in ABAQUS/Standard, as shown in Fig. 5. The matrix material is modelled by isotropic von-Mises plasticity with a stress-strain relationship shown in Fig. 4. The inner planes of symmetry are fixed against normal displacements, while all outer planes are only allowed to move rigidly in the corresponding coordinate directions. The cell model is loaded with macroscopic stress by means of pressure loads on the outer planes, the proportion of which are carefully calculated to realise a wide range of stress triaxiality T, from 0.6 to 2.0.

The void volume fraction, the macroscopic equivalent stress and strain can be calculated with equations in [10]. Figure 6 plots the void volume fraction against the equivalent strain under different stress triaxiality. The points after which void growth is linearly accelerated mark the unstable void growth and the onset of void coalescence, and thus are regarded as the critical strains for tension fracture. Figure 7 shows the dependence of tension fracture strain, ε_f^t, on stress triaxiality, which can be represented by an exponential function:

$$\varepsilon_f^t = Ce^{-D \cdot T} \tag{10}$$

Comparing to many widely adopted tension fracture models that were based on the Rice-Tracey void growth equation, such as those in [11] and [12], Eq. (10) does not employ the fixed exponent of -1.5, but incorporates another free parameter D to generate a more general model for application in various metallographically different metals. For example, the above cell model study indicated an exponent of -1.75 when the stress-strain relationship of the matrix material is assumed as Fig. 4, but an exponent of -2.0 when an ideally plastic matrix material is assumed.

3.3 Shear fracture criterion

Voids nucleate at locations where the local stress is built up to a critical value. Argon et al. gave the most widely accepted continuum model to describe the formation of void [7], in which the critical local stress σ_c is calculated as $\sigma_c = \sigma_h + \sigma_{eq}$. Most metal materials including constructional steels follow the Hollomon's power law equation, and therefore, the equivalent plastic strain for voids to nucleate, ε_{nc}, is:

$$\varepsilon_{nc} = \frac{\varepsilon_c}{(T+1)^{\frac{1}{n}}} \tag{11}$$
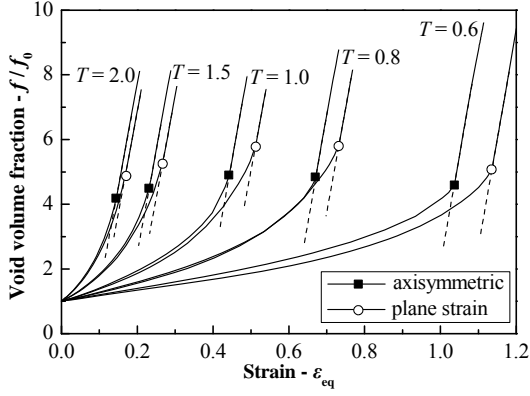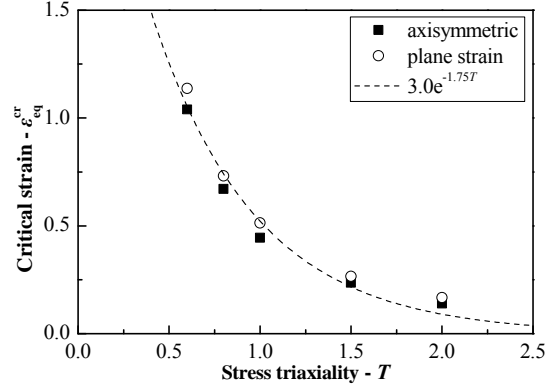
Fig. 6 Void volume fraction in high triaxiality.

Fig. 7 Critical strain in high triaxiality.

Finite-element unit cell-based micromechanical study can also be employed to investigate the void collapse behaviour, in which Lode parameter L, defined as $L=(2\sigma_2 - \sigma_1 - \sigma_3)/(\sigma_1 - \sigma_3)$, is also considered as it was found to affect the shear fracture; in actuality, the stress state of a material point can only be uniquely described by using both the stress triaxiality and Lode parameter. In this study, the stress triaxiality ranges from –0.3 to 0.3 with an interval of 0.1, and the Lode parameter ranges from –1 to 1 with an interval of 0.25.

Figure 8 demonstrates the void deformation in low positive and negative triaxiality. In most cases voids experience an abrupt collapse instead of a dramatic size growth as that is observed in high triaxiality. The collapse strain ε_{cl}, namely, the strain when the void vanishes completely, is dependent on both T and L, which can be represented by Eq. (12) and is shown in Fig. 9.

$$\varepsilon_{cl} = p_1 + p_2 e^{p_3 T - p_4 L} \tag{12}$$

Substituting Eqs. (11) and (12) back to Eq. (9), we get:

$$\varepsilon_f^s = \frac{q_1 + e^{q_3 T - q_4 L}}{q_2 (T+1)^{\frac{1}{n}}} \tag{13}$$
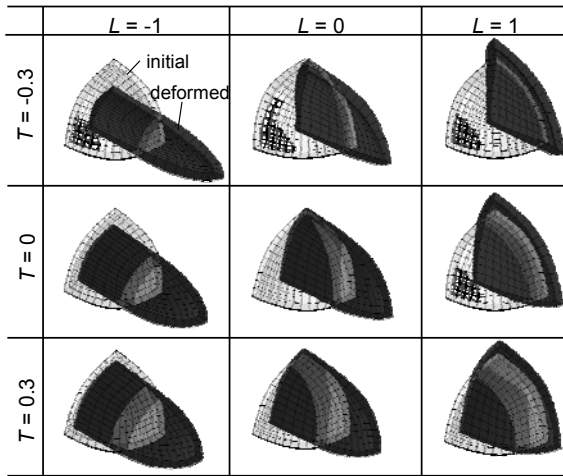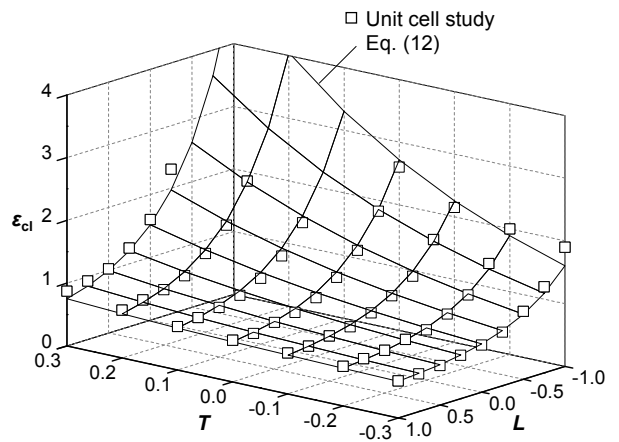

Fig. 8 Void collapse in low triaxiality.

Fig. 9 Critical strain in low triaxiality

7

Free parameters q_1 to q_4 can be calibrated by tests of at least four coupons that generate different stress states. This is cost inefficient. Many coupon tests demonstrated that in plane stress space the ductility under pure shear, i.e., $T=0$, $L=0$, is the local minima [13]. This condition writes q_2 as a function of q_3 and q_4. Meanwhile, based on the above finite-element unit cell study, a small positive value, 0.4, is adopted for q_4 to consider the influence of Lode parameter. Therefore, Eq. (13) becomes:

$$\varepsilon_{\mathrm{f}}^{\mathrm{s}} = \frac{An+n-1+e^{A\cdot T-0.4L}}{B\cdot(T+1)^{\frac{1}{n}}}, \text{ with } A > \frac{1}{n}-2 \tag{14}$$

3.4 The overall fracture model

An overall fracture model can be defined by combining the fracture criteria obtained in Sections 3.2 and 3.3 while distinguishing the tension and shear fracture modes. As no void nucleates when $T \le -1$, the overall fracture model is written as:

$$\varepsilon_{\mathrm{f}} = \begin{cases} +\infty & T \le -1 \\ \min\left(\varepsilon_{\mathrm{f}}^{\mathrm{s}}, \varepsilon_{\mathrm{f}}^{\mathrm{t}}\right) & T > -1 \end{cases} \tag{15}$$

The model can be validated using the coupon tests in [13], which included fifteen different 2024-T351 aluminium alloy coupons covering a wide range of stress triaxiality, as shown in Fig. 10. The validation strategy is to use a necessary amount of tests for calibration of the free parameters, and then use the other tests to check the accuracy of the calibrated model. The shear and tension branches of the model are calibrated separately. From Tests #3 and #15, tensile fracture parameters C and D are calculated as 0.59 and 1.40, respectively. In order to reduce the number of necessary tests in calibrating the shear fracture parameters A and B, a simple presumption is introduced that in plane stress space the shear and tension branches are divided by the uniaxial tension state, i.e., $T=1/3$. Thus, using Test #10 and the already calibrated tension branch, the shear fracture parameters A and B are calibrated as 6.52 and 5.49, respectively. It is observed in Fig. 10 that the calibrated fracture model gives excellent prediction of all test results.
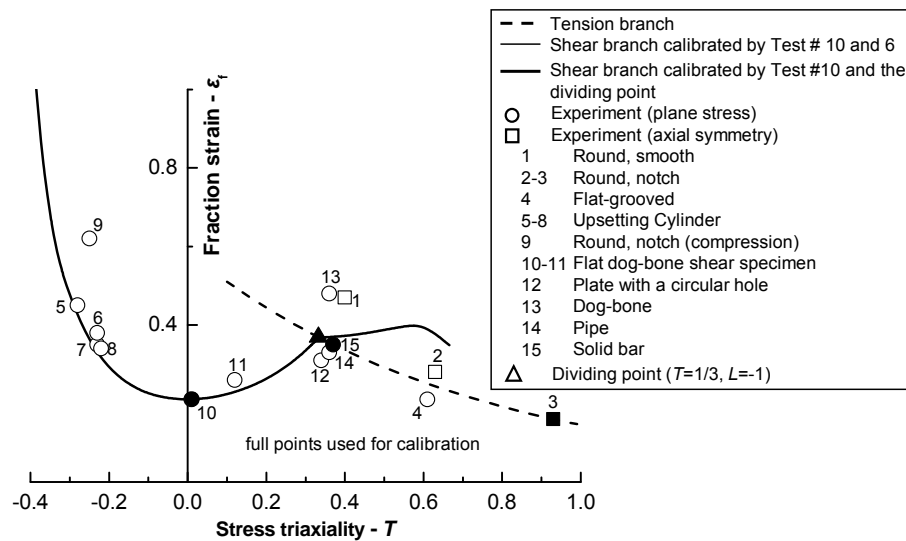

Fig. 10 Fracture model validation the using the test results in [13].

8

4. NUMERICAL SIMULATION METHOD OF FRACTURE

Finite-element solvers that are based on implicit time integration encounter numerical troubles when fracture of material is involved, where fractured elements are to be deleted from the finite-element mesh.

A pseudo element deleting method is put forward in this study, in which elements are deleted indirectly by means of reducing the Young's Modulus of these elements down to zero, generating elements with no stress but having infinite deformability. This study adopts finite-element package ABAQUS/Standard, in which user subroutine USDFLD can be used to reduce the Young's Modulus of integration points to 1.0 MPa (in finite-element solvers material properties must be positive) when fracture of these integration points are detected. Material softening may cause local instabilities and convergence difficulties. At this time, the technique provided by ABAQUS/Standard for stabilizing local unstable quasi-static problems can be employed, which adds volume-proportional damping to all elements. Moreover, it is desirable to increase the numbers of iterations in each incremental step in a Newton method, because the force residual of iteration is not always monotonously reduced when there is material softening.

Another significant issue is the characteristic length of material, i.e., the size of elements where fracture is expected. In this study, the characteristic length is determined as the dimension of plateaus and valleys on the castellated fracture surface, as suggested in [11, 12]. Keyence VHX-2000 Digital Microscope was used to measure the microstructures of fracture surfaces of Q345 tension coupons, showing an average characteristic length of about 0.25 mm, as shown in Fig. 11.
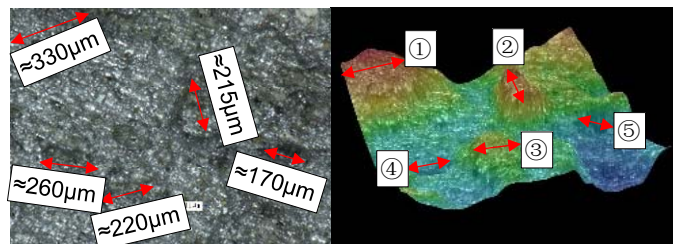

Fig. 11 Characteristic length measurement.

5. PARAMETER CALIBRATION FOR Q345 GRADE STEEL

5.1 Coupon tests

Seven coupon types made from Q345 grade steel were tested to calibrate the proposed fracture model. As shown in Fig. 12, these coupon types included notched round bar coupon with a respective circumferential notch radius of 10 mm (NRB10), 5 mm (NRB5) and 0.5 mm (NRB0.5), rectangular solid bar coupon (RSB), and shear coupon with a respective angle of 0º (S0), 30º (S30) and 60º (S60) between the loading direction and the central weaken region. All coupons were cut from the same steel plate as the SRB coupons in Section 2. For each coupon type, three coupons were tested to obtain an average force-deformation curve.

Figures 13-15 show the force-displacement curves obtained from the tests. Special attention was paid to shear fracture, and Fig. 16 shows the fracture process of the S0 coupon. Plastic deformation was highly localized in the weaken region, and fracture initiated at the centre of the region and propagated rapidly along the shear direction, leading to a straight while slightly tilted crack.
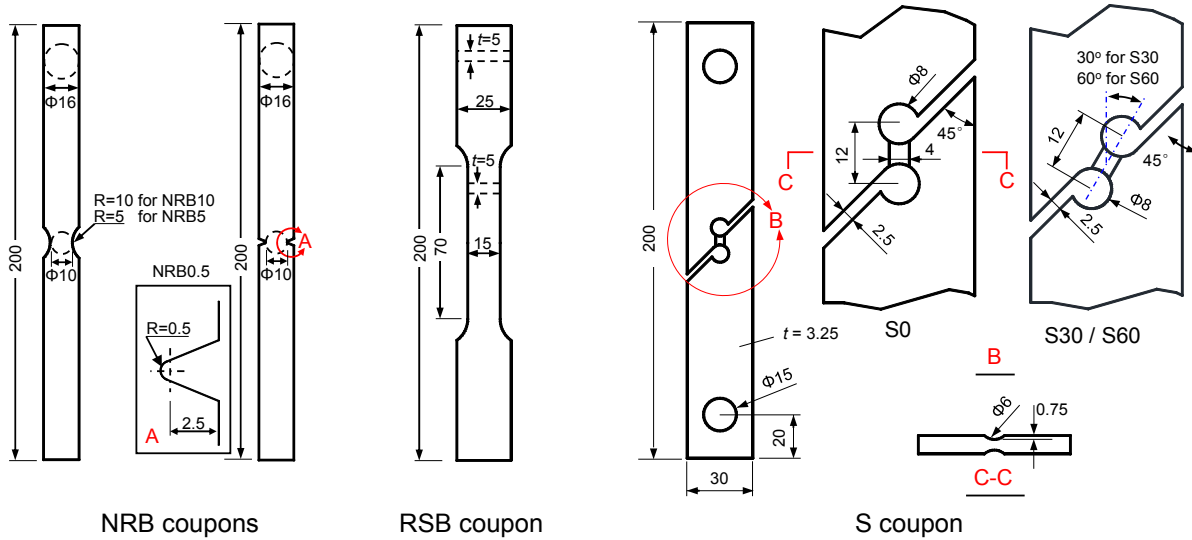
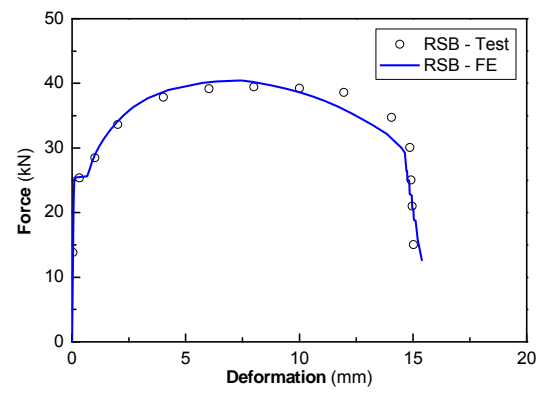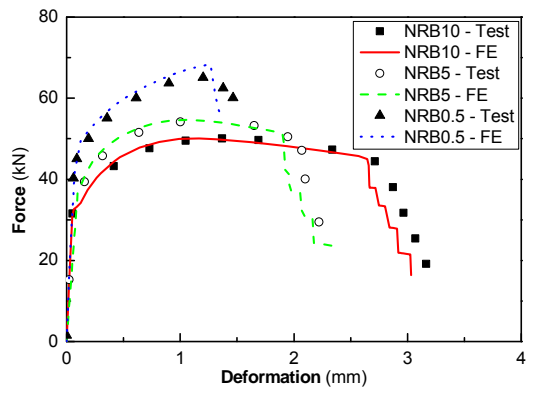Fig. 12 Geometries of coupons (unit: mm).

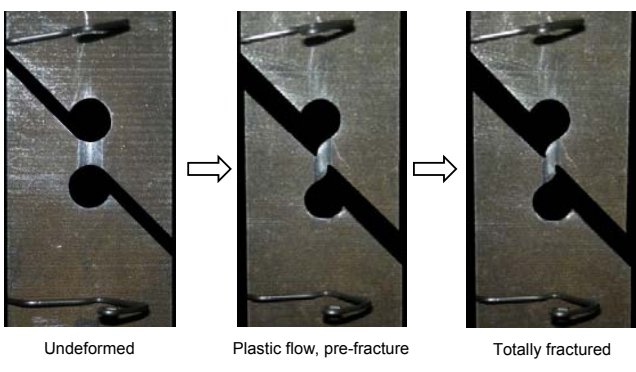Fig. 13 Force-deformation curves of NRB coupons. Fig. 14 Force-deformation curve of RSB coupon.
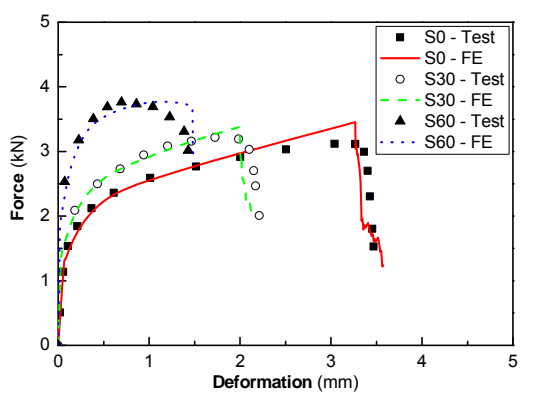

Fig. 15 Force-deformation curves of S coupons. Fig. 16 Deformation and fracture of S0 coupon.

5.2 Model calibration and validation

To calibrate the free parameters in the fracture model, at least three pairs of fracture strain-stress state relationship are needed, which can be obtained from NRB5, RSB and S0 tests. Coupon test provided information about the location of fracture initiation and the moment of fracture initiation (the pulling force began to drop abruptly), but gave no information of the

plastic strain and stress state at the fracture initiation location. Numerical simulations were performed for the interpretation of the test results.

Figure 17 illustrates the finite-element models developed in ABAQUS/Standard. The material is modelled with a stress-strain relationship shown in Fig. 4, but fracture model is not included. The plastic strain and stress state at the fracture initiation location are obtained. Note that stress state varies during loading, and thus the average stress triaxiality and Lode parameter are used to characterize the equivalent stress state for fracture strain ε_f, which is the equivalent plastic strain at the moment of fracture.

NRB5 and RSB showed a ε_f -T relationship of {T=0.86, ε_f=0.34} and {T=0.44, ε_f=1.16}, respectively, and S0 showed a ε_f -T-L relationship of {T=0.02, L=−0.07, ε_f=0.89}. Stress-strain relationship in Fig. 4 had a strain hardening exponent n=0.145. Using the model calibration method in Section 3.4, we get A=7.08, B=1.38, C=4.25 and D=2.95 for Q345 grade steel.
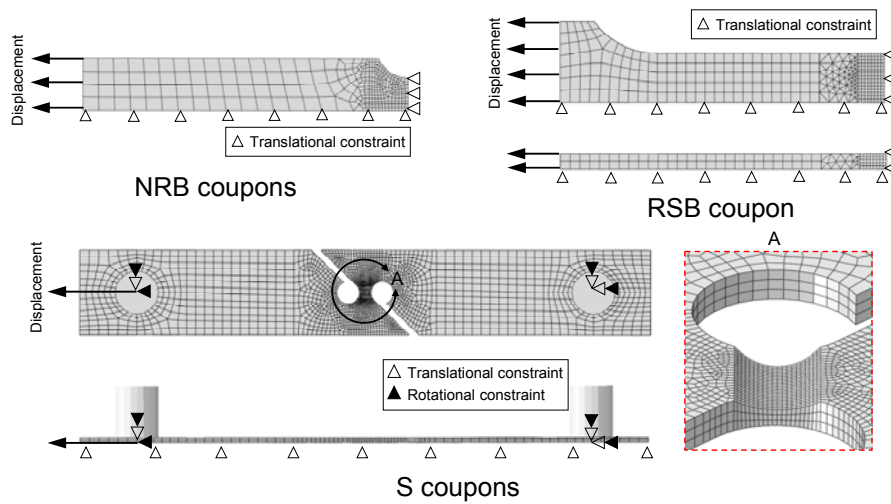

Fig. 17 Finite-element models of the coupons.

Numerical simulation of all coupon tests are performed with the calibrated fracture model embedded in ABAQUS/Standard through user subroutine. The simulation results are already shown in Figs. 13-15 and are compared against the test results. It is observed that numerical simulations give excellent predictions on both the fracture initiation and propagation. Figure 18 depicts the fracture process of S0 coupon predicted by the simulation, which is in good agreement with the experimental observation shown in Fig. 16.

6 CONCLUSION

This paper presents a comprehensive study that aimed to provide a useful tool for numerically predicting the fracture phenomenon in steel structures, including the method for determining the yield-to-fracture true stress-strain relationship, a micro-mechanism-based fracture model, and the numerical method for fracture simulation. Comparisons between the experimental and numerical results showed that the proposed model and methods had excellent performance in predicting the fracture initiation and propagation, indicating that the model and methods proposed in this study are ready for future application in large-scale structural engineering problems.
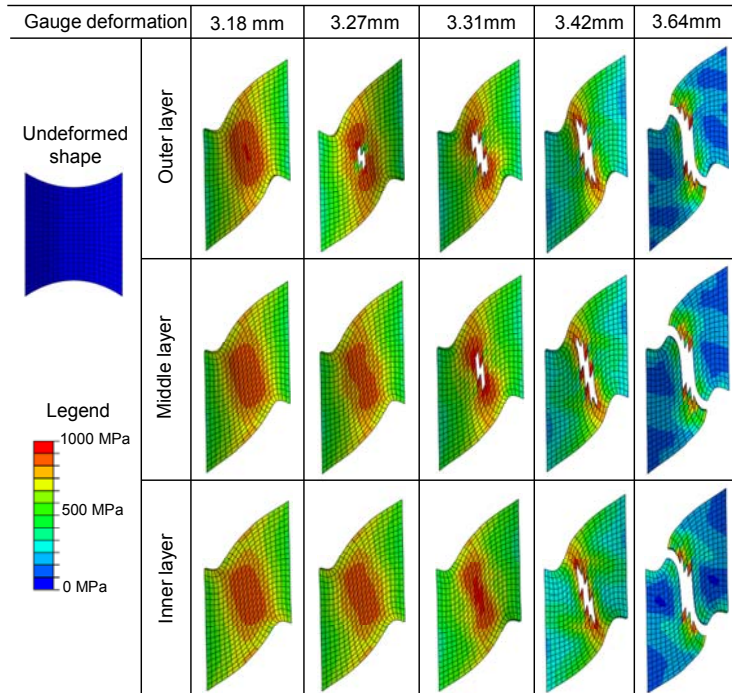
Fig. 18 Fracture simulation of S0 coupon.

REFERENCES

[1] Yan S. *Progressive collapse research of large-span space frame structures*. PhD thesis submitted to Tongji University, 2015.

[2] Yan S, Zhao X and Wu A. Ductile fracture simulation of constructional steels based on yield-to-fracture stress-strain relationship and micro-mechanism based fracture criterion. *J Struct Eng*, 2018, 144(3): 04018004.

[3] Yan S. and Zhao X. A fracture criterion for fracture simulation of ductile metals based on micro-mechanisms. *Theor Appl Fract Mec*, 2018, 95: 127-142.

[4] Bridgeman DW. *Studies in Large Plastic Flow and Fracture*. New York, McGraw Hill, 1952.

[5] *GB 50017-2003, Code for Design of Steel Structures*. Ministry of Construction of the People's Republic of China, Beijing, 2003.

[6] Anderson TL. *Fracture Mechanics - Fundamentals and Applications, second ed*. CRC press, New York, 1997.

[7] Argon AS, Im J and Safoglu R. Cavity formation from inclusions in ductile fracture. *Metallurgical Transactions A*, 1975, 6: 825-837.

[8] Beremin FM. Cavity formation from inclusions in ductile fracture of A508 steel. *Metallurgical Transactions A*, 1981, 12: 723-731.

[9] Danas K and Ponte Castañeda P. Influence of the Lode parameter and the stress triaxiality on the failure of elasto-plastic porous materials. *Int J Solids Struct*, 2012, 49: 1325-1342.

[10] Kuna M and Sun DZ. Three-dimensional cell model analyses of void growth in ductile materials. *Int J Fracture*, 1996, 81: 235-258.

[11] Hancock JW and Mackenzie AC. On the mechanisms of ductile failure in high-strength steels subjected to multi-axial stress-states. *J Mech Phys Solids*, 1976, 24: 147-169.

[12] Kanvinde AM and Deierlein GG. Void growth model and stress modified critical strain model to predict ductile fracture in structural steels. *J Struct Eng*, 2006, 132: 1907-1918.

[13] Wierzbicki T, Bao YB, Lee YW and Bai YL. Calibration and evaluation of seven fracture models. *Int J Mech Sci*, 2005, 47: 719-743.